applied sciences

MDPI

Article

Multiobjective Optimization for the Aero-Structural Design of Adaptive Compliant Wing Devices

Alessandro De Gaspari

Department of Aerospace Science and Technology, Politecnico di Milano, Via La Masa 34, 20156 Milano, Italy; alessandro.degaspari@polimi.it

Received: 14 August 2020; Accepted: 10 September 2020; Published: 13 September 2020

Abstract: The design of morphing structures must combine conflicting structural requirements and multiple load conditions that are related to the aerodynamic shapes aimed at optimizing aircraft performance. This article proposes a multilevel approach for the design of adaptive compliant wing devices. A set of aerodynamic shapes, and associated their loads, is defined by a shape optimization, coupled with a three-dimensional parametric technique, that can identify only feasible shape changes due to the morphing. A topology and sizing multiobjective optimization drives the Pareto-optimal structural design of the compliant structure, which is able to deform itself to match, once actuated, all of the previously defined aerodynamic shapes. Next two design levels produce a more detailed solution which is extended until the definition of the complete device. A 90 pax, twin prop green regional aircraft is used as an innovative aircraft demonstration platform for the design of the morphing droop nose to be installed on the wing. The results show the structural capabilities of this device in terms of the external shape quality and the strain requirements. This work enables the validation of the design method and prove the functionality of compliant structures when accounting for the aeroelastic effects due to the interaction with the wing-box.

Keywords: morphing; wing devices; multiobjective optimization; compliant structures; pareto-optimal; aeroelasticity

---

1. Introduction

Adaptive aircraft structures can provide many benefits related to the capability of continuously modifying and optimizing the aerodynamic wing shape across the flight envelope. According to the classification of morphing [1], one of the most pursued concepts is active camber morphing, which aims to replace conventional flight control surfaces installed on fixed wing aircraft. Substituting classical hinged or slotted leading and trailing edge devices with flexible structures is an attractive goal due to the effective benefits that can be achieved in terms of flight and aerodynamic performances. The main goal is the reduction of fuel consumption and acoustic emissions during the mission [2,3].

The design of conventional aircraft wings is the result of an optimization process based on a single flight condition, typically the cruise, at a given speed and altitude. Aircraft performances are suboptimal in the other conditions. If there was the possibility of changing the wing shape on demand, near-optimal performances for different conditions could be achieved. This goal is the idea behind the morphing concept, which is based on adaptive structures. According to the NATO RTO Technical Team on Morphing Vehicles, morphing is the “real-time adaptation to enable multi-point optimized performance” [4]. Weisshaar [5] suggested that “morphing aircraft are multi-role aircraft” that can change their external shape to adapt to a changing mission environment during flight. Most real-world aeronautical design problems involves multiple load conditions. In the case of the design of adaptive structures, there is also a need to combine conflicting structural requirements. This complexity can be summarized in the morphing paradox: the same structure must be sufficiently stiff to withstand its external loads without suffering appreciable deformations, and it must be flexible enough to change its shape into the required shape [6]. In this sense, many authors have described the morphing challenge. The design of adaptive structures becomes critical when it concerns control surfaces, because they must be designed as aeronautical structures that can achieve large deformations that are localized in small regions of the wing. On the one hand, they must be able to change the aerodynamic performance at different conditions of the flight envelope and to provide highly variable aerodynamics distributions, as required by the design manoeuvres. On the other hand, when the morphing device is actuated, the adaptive structure must be able to change its shape while being insensitive to load variations. The multi-load-bearing capability of the control surfaces implies that the external shape cannot be affected by the load variation. Adaptive structures are used as control surfaces, but they must be designed as structures, and thus the determination of the loads acting on the aircraft is one of the main tasks during their design. The knowledge of loads is important for structural design, prediction of the performance, and certification. Wright and Cooper [7] wrote: "Aircraft are subject to a range of static and dynamic loads resulting from flight manoeuvres, ground manoeuvres and gust/turbulence encounters." These load cases influence the structural design and should be recomputed for each considered mass state across the flight envelope [8]. Considering all of the load cases is not possible due to computational constraints, and thus some type of downselection must be implemented to identify a reduced set of critical load cases. Different approaches have been proposed in the literature. The most common methods are load envelopes, which are typically based on maximum and minimum criteria. More recent methods are based on using singular value decomposition to derive a set of characteristic loads that approximate all of the global load distributions [9]. For a realistic design, internal loads must be calculated for a few tens of characteristic loads rather than thousands of real load cases. A smaller number is usually required for the design of control surfaces. Moreover, many manoeuvre loads depend on trim conditions, which imply the availability of a flight simulator of the aircraft, something that is not possible when the structural design begins, especially in a fly-by-wire control system [10]. Modern design approaches are based on decoupling the load analysis from the flight control laws design. These methods represent an agreement between the loads and flight mechanics, where the former analyses the boundaries of a predefined envelope for the structural design and the latter ensures that the flight control laws do not work outside this area [11,12]. A similar approach is presented in this article for the design of adaptive structures, where multiple loads depend on the aerodynamic shapes that the morphing device can achieve, which are unknown when the design begins. The idea is to define aerodynamic shapes that can maximize the aircraft performances before, and then to design an adaptive structure that can match, once actuated, all of the aerodynamic shapes previously defined, while accounting for the conflicting structural requirements mentioned above.

Most of the work in the literature on morphing deals with performance optimization [13,14], modeling of morphing wings [15], and design of specific morphing devices [16–18]. On the one hand, the issue related to multiple load conditions and conflicting structural requirements needs a dedicated design methodology, and, on the other hand, other open issues are related to the Technology Readiness Level (TRL). The technology maturity of the adaptive structures concerns the estimation of overall benefits that should overcome the weight and complexity penalty [1]. More specific issues concern the integration between the actuation, morphing devices, and existing wings [13], and the design of flexible skins that cannot be considered too innovative with respect to the materials, to be installed on the modern aircraft. Adaptive structures represent conformable and gapless control surfaces that can be attached to the traditional wing-box. This approach is a clear advantage for strength-to-weight ratio considerations and because of the need for fuel storage. This morphing solution can be accepted by industries and certification boards and organizations, but the aeroelastic effects and the mutual interactions, in terms of the functionality and accuracy of the target deformed shape, must be evaluated. Concerning the deformable skin, the most critical aspect is that the external shape must be kept smooth in order to not compromise the aerodynamic efficiency, without exceeding the material strain limits.

The structural solution proposed in this article for the design of adaptive structures is based on the distributed compliance concept. This concept was originally proposed by Kota [19], as an alternative to the distributed actuation concept, and then it was successfully adopted by Politecnico di Milano (PoliMi) in many European projects, as the basis for the design of morphing wings [20] and wind tunnel models equipped with adaptive compliant leading and trailing edges [21]. Compliant structures are optimized to efficiently distribute the flexibility in the structure and to transform the input actuation energy into strain energy to achieve the desired motion or the required shape change. They have been shown to be suitable for realizing seamless and gapless wing control surfaces and do not require the use of unconventional actuators or excessively innovative skin solutions [22].

Due to the peculiar characteristics of compliant structures, dedicated design procedures must be developed, and specific tools are required, to achieve a feasible design. An intensive research activity that was conducted over the past ten years at PoliMi, has led to the continuous development of a design procedure based on the two-level approach described in [23]. However, the design of adaptive structures is a naturally multiobjective optimization problem (MOOP). Starting from here, a new procedure based on a multiobjective algorithm that can address conflicting structural requirements and multiple load conditions is presented in this article. Due to the conflicting multiple objectives, the results of the MOOP consist of a number of optimal solutions, known as Pareto-optimal solutions or non-inferior solutions [24]. They represent all of the possible and feasible compliant structure solutions that can match all of the aerodynamic shapes that were previously defined. This procedure is based on a multilevel approach that allows a more accurate design of the compliant structure, while accounting for a complete and three-dimensional device representation.

The complete optimization procedure has been applied to the design of a morphing droop nose to be installed on the Green Regional Aircraft (GRA), provided by Leonardo company and used as an Innovative Aircraft Demonstration Platform (IADP) inside the Clean Sky 2 REG-IADP AirGreen2 (AG2) project. This study also aims at evaluating the interaction between the morphing device and the existing wing-box, while considering the flexibility of the wing and evaluating the static aeroelastic equilibrium. This is an important aspect that is not covered in the literature on morphing droop nose [16,25,26].

This article is organized as follows. Section 2 describes the multiobjective optimization approach for the synthesis of adaptive compliant structures, which represents the foundation of the proposed multilevel design procedure described in Section 3. Section 4 describes the IADP and introduces the innovative droop nose to be installed on the Green Regional Aircraft. Section 5 reports the results obtained by applying the procedure to the design of the adaptive compliant droop nose. Finally, the conclusions of this work are presented in Section 6.

2. Multiobjective Optimization of Compliant Structures

Methods for solving MOOPs can be distinguished into classical methods and evolutionary algorithms (EA). In general, classical methods need some information about the preferences of each objective or on the algorithmic parameters to find a single Pareto-optimal solution. Due to the complexity in solving a MOOP, it is usually converted into a single-objective optimization problem. The weighted sum method scalarizes the problem by defining a single objective function that results from the dot product of a user-supplied weight vector and the vector that contains all of the objective functions. This approach is the simplest and most widely used classical method, but it poses an issue that is related to the values to be assigned to the weights. They depend on the importance of each objective function, and, at the same time, on the normalization that must be conducted to make the objectives of the same order of magnitude to be considered equally in the solution. The values of these weights vary from problem to problem and, in general, predicting the appropriate weighting factors is impossible. Two interesting theorems from Miettinen [27] state that a solution obtained by the weighted sum method is Pareto-optimal if all weights are positive, which has also been confirmed for convex problems. Multiple Pareto-optimal solutions can be found by repeating the same single-objective optimization and each time changing the positive weight vector. This approach does not mean that different weight vectors lead to different Pareto-optimal solutions because some solutions could be dependent on one another. Finally, to find m Pareto-optimal solutions, at least, if not more than, m different single-objective optimizations must be performed. Weighted sum methods do not definitively guarantee being able to find the Pareto-optimal solutions in the whole Pareto-optimal domain. In addition to these disadvantages, classical methods are affected by typical problems of direct and gradient-based optimization algorithms: they can fall into a locally optimal solution, cannot be parallelized, and the solution's convergence depends on the initial solution.

On the other hand, EAs offer significant advantages when they are used to solve MOOPs, due to their capability to process an entire population of solutions in each generation. Therefore, a population of Pareto-optimal solutions is potentially captured after each generation, and increasing the initial population size allows us to capture as many Pareto-optimal solutions as possible. This eliminates the dependency on external parameters, such as weight vectors, and does not require repetitive use of single-objective optimizations to obtain Pareto-optimal solutions that could be weakly dominated by each other, which wastes computational effort. EAs can preserve the diversity of multiple non-dominated solutions inside the population during the entire process that gradually converges to the Pareto-front, ensuring a good spread and providing many different optimal solutions [24].

The synthesis of compliant mechanisms is the design of a particular type of structure that can convert a displacement or a force from an input point (actuator) to an output point to a different direction, using the deformation work efficiently. It is a mechanical component design problem that is usually solved as a single-objective optimization problem. The objective represents a kinematic requirement, such as the maximization of the motion or the force amplification. However, this kind of problem should be better posed as a minimum two-objective optimization problem. On the one hand, a compliant mechanism designed only to be flexible can meet kinematic requirements through deformation, but it could be too flexible to bear external loads. On the other hand, a compliant mechanism designed only to bear external loads could meet structural requirements but could require too much force to achieve a desired motion, producing high stresses as a result. Therefore, the design must be decomposed into a kinematic (for motion) and structure (for load-carrying capabilities) design problem that are simultaneously considered. This task can be accomplished in different ways, by using different objective functions. Lu and Kota describe the most common objective functions for the design of Single-Input Single-Output (SISO)-compliant mechanisms and suggest how they can be combined in a single-objective optimization [28]. If the strain energy is to be minimized and the mutual energy is to be maximized, individual optimization problems can be formulated as described in Sections 2.1 and 2.2, respectively.

The synthesis of a compliant structure is a Single-Input Multi-Output (SIMO) design problem where the actuation input is converted into deformation energy to deform the contour skin. In this case, the kinematic design is more appropriately defined as a shape-adaptable design problem, as described in Section 2.3. Moreover, a multiobjective problem should be considered to combine a pair of kinematic and structural designs for each load condition included in the set of selected load cases, as described in Section 1. This problem increases its complexity when the adaptive structures are used to replace the control surfaces that should be insensitive to load variations. The importance of the structure objective function is comparable to the kinematic objective function, and, as a result, the Pareto-optimal design described in Section 2.4 is the only correct way to proceed for the synthesis of compliant structures. This article presents a new approach for the design of compliant structures based on Genetic Algorithms (GAs) working on a population of Pareto-optimal solutions.

2.1. Kinematic Design

The first part of the conflicting objective functions is the mechanism design that is first formulated for the synthesis of a SISO-compliant mechanism. Maximizing the deflection at the output point is equivalent to maximizing the Mutual Potential Energy (MPE) [29]: the structural topology that maximizes the output displacement is found by maximizing the strain energy, which is equal to the virtual work of the system, while considering the solutions of two equilibrium equations: $\mathbf{u}_{in}$, which is the nodal input displacement vector due to the actuator input force $\mathbf{f}_{in}$, and $\mathbf{u}_{out}$, which is the nodal output displacement vector due to the arbitrary fictitious force $\mathbf{f}_{out}$ with direction and orientation equal to the displacement to be maximized.

The concept of MPE is the mutual energy of a system due to the two different sets of loads with the same boundary conditions, as shown in Figure 1. The optimal problem formulation, which corresponds to the maximization of the MPE, can be stated as follows,

$$\max_{\mathbf{u},\, E_e} \; \mathbf{u}_{out}^T \mathbf{K}(E_e) \mathbf{u}_{in} \tag{1}$$

such that

$$\begin{aligned} \mathbf{K}(E_e)\mathbf{u}_{in} &= \mathbf{f}_{in} \\ \mathbf{K}(E_e)\mathbf{u}_{out} &= \mathbf{f}_{out} \\ E_e &\in \mathrm{E}_{admissible} \end{aligned}$$

where $\mathbf{K}(E_e)$ is the symmetric global stiffness matrix, which depends on the element stiffness E_e with $e = 1, \cdots, N$, and N is equal to the number of finite elements that the design domain has been discretized into.

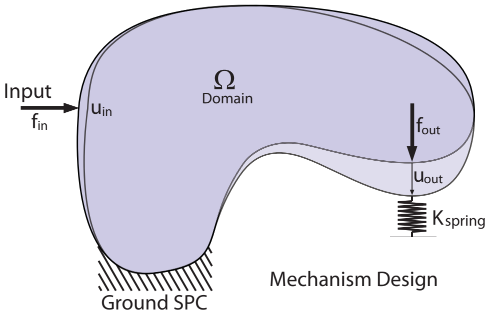

Figure 1. Mechanism design: compliance for desired motion.

2.2. Structure Design

The first part of the conflicting objective functions is the structure design, which employs the simplest type of design problem formulation in the topology optimization field, namely, *minimum compliance design* (maximum global stiffness) [30]. Maximizing the stiffness is equivalent to minimizing the strain energy (SE) of a system, as shown in Figure 2, where the input point is fixed, and the load is applied at the output point in the opposite direction, while accounting for the resistance of the compliant structure to be designed.

The system corresponds to a single equilibrium equation and the optimal problem formulation can be stated as follows,

$$\min_{\mathbf{u},\, E_e} \; \mathbf{u}_{out}^T \mathbf{K}(E_e) \mathbf{u}_{out} \tag{2}$$

such that

$$\begin{aligned} \mathbf{K}(E_e)\mathbf{u}_{out} &= -\mathbf{f}_{out}, \quad \textit{with } SPC_{in} \\ E_e &\in \mathrm{E}_{admissible} \end{aligned}$$

where $\mathbf{u}_{out}$ is the nodal output displacement vector due to the force $-\mathbf{f}_{out}$, and $\mathbf{K}$ is the symmetric global stiffness matrix, as in the previous problem.

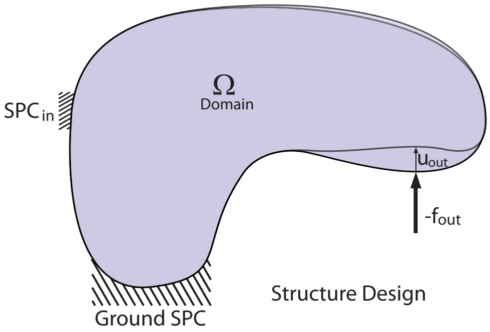

Figure 2. Structure design: stiffness to bear loads.

2.3. Shape-Adaptable Design

The design of SIMO systems is called *synthesis of path-generating mechanisms* [30]. The kinematic problem is defined as the minimization of the error, in a least square sense, between the deformation of the compliant mechanism once actuated and a target shape previously defined. A comparison between the two shapes is performed for a discrete number of control points distributed over the contour to be deformed. If the contour is discretized, as in the case of a finite element model, the problem requires the output points to pass through a number K of points $\bar{\mathbf{u}}_{out}$, defined by the designer. The topology optimization can be written as follows,

$$\min_{\mathbf{u},\, E_e} \sum_{i=0}^{K} \alpha_i \sum_{k=1}^{K} \left(\mathbf{u}_{out,k,i} - \bar{\mathbf{u}}_{out,k}\right)^2 \tag{3}$$

such that

$$\mathbf{K}(E_e)\mathbf{u} = \mathbf{f}$$
$$E_e \in \mathrm{E}_{admissible}$$

where $\mathbf{u}_{out}$ is a subset of the displacement vector $\mathbf{u}$, and $\mathbf{f}$ is the nodal force vector, including the actuator input force $\mathbf{f}_{in}$ and the external loads. Unlike what has been done in the cases in Section 2.1, for multi-output mechanisms, it does not make sense to attach a spring at the output point to ensure an efficient force transfer. However, if the external loads are applied to the output points, weighting factors α_i can be used for the output displacement $\mathbf{u}_{out,k,i}$. More specifically, the circumstances could be with no counter load $i = 0$, with a counter load against the output path $i = 1$, or with a counter load perpendicular to the output path $i = 2$ [31,32].

The synthesis of path-generating mechanisms can be used for the design of adaptive structures. Unlike the SISO problems, in the adaptive shape problems the quality of the solutions depends on the precise deformation of several discrete output points placed along the shape-adaptable boundary, as shown in Figure 3.

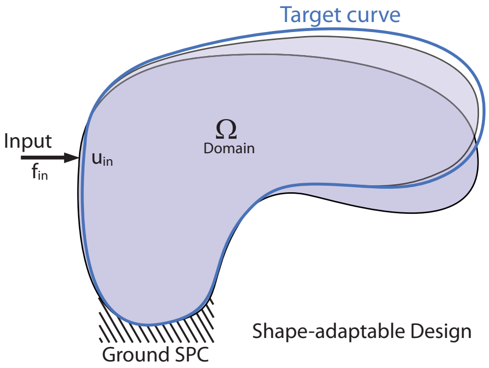

Figure 3. Shape-adaptable design: compliance for desired shape adaptation.

2.4. Pareto-Optimal Design

In the case of conflicting objectives and multiple load cases, the design of an adaptive structure can be conducted by solving a multiobjective optimization problem in which a number of M shape-adaptable designs (3), which correspond to M different load conditions, are combined with a number of N structure designs Figure 2, which correspond to N different load conditions. The multiobjective topology optimization can be written as follows,

$$\begin{aligned} &\min_{\mathbf{u},\,E_e} \sum_{i=0}^{K} \alpha_i \sum_{k=1}^{K} \left(\mathbf{u}_{out,m,k,i} - \bar{\mathbf{u}}_{out,m,k}\right)^2 \quad m = 1, 2, \ldots M; \\ &\min_{\mathbf{u},\,E_e} \mathbf{u}_n^T \mathbf{K}(E_e)\mathbf{u}_n \quad n = 1, 2, \ldots, N; \end{aligned} \tag{4}$$

such that

$$\begin{aligned} \mathbf{K}(E_e)\mathbf{u}_m &= \mathbf{f}_m \quad m = 1, 2, \ldots M; \\ \mathbf{K}(E_e)\mathbf{u}_n &= \mathbf{f}_n \quad \mathit{with}\ SPC_{in}, \quad n = 1, 2, \ldots\ N \\ E_e &\in \mathrm{E}_{admissible} \end{aligned}$$

In this case, a set of Pareto-optimal solutions is obtained and the design point can be selected in the Pareto-front. If any other information is available, then all Pareto-optimal solutions are equally important. If higher-level information is available, it can be used by post-optimal decision-making techniques.

3. The Multilevel Approach

The design of a shape-adaptable compliant structure is a complex problem, due to its multiobjective nature, including conflicting requirements. Moreover, the design from scratch must combine different types of optimization, such as topology, shape, and sizing optimizations. For this reason, the design is broken down into a series of simpler problems, by identifying the relationships between the design variables, objectives, and constraints that allow them to be separated into interconnected groups. The overall optimization becomes a multilevel optimization process that gives additional advantages. Due to the multidisciplinary nature of the whole design process, each level corresponds to an individual disciplinary optimization. Increasing the model fidelity can be adopted through different levels, and the results obtained by the multiobjective GA can be refined to perform local optimization. A schematic representation of the multilevel procedure is shown in Figure 4.

The first-level consists of an aero-structural shape optimization that can produce a number of morphing shapes that correspond to the set of multiple load cases. The goal is the definition of the optimal morphing shape according to the performance requests. Additionally, structural constraints assure the feasibility of the shape solutions from the point of view of the stress within the skin.

In the second-level optimization, solutions that come from all morphing shape optimizations are grouped together and used as target shapes by a dedicated multiobjective genetic algorithm. This optimization level defines the topology of the internal compliant structure and produces a two-dimensional conceptual solution that can deform itself by matching all of the aerodynamic shapes defined by the first level.

The third level is a local optimization that is used to refine the sizing and geometry design that arises from the second level, working on three-dimensional finite element models of increased fidelity. This level adapts the internal structure topology solution to different sections along the wing span.

The fourth level aims at generating a three-dimensional high-fidelity model of the complete morphing device, which can perform virtual testing and be virtually installed on the wing-box to evaluate mutual interactions. This level allows us to make the design close to the manufacturing and experimental tests.

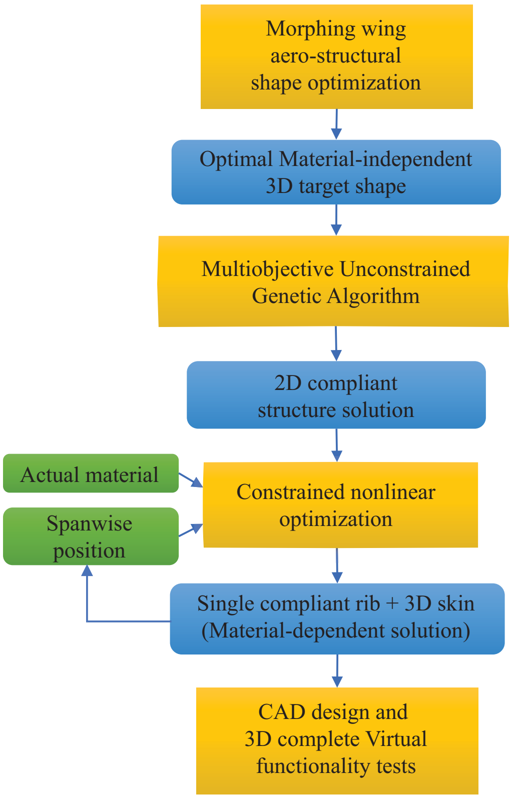

Figure 4. Multilevel optimization procedure.

3.1. First Level

The first level of the procedure consists of an aerodynamic shape optimization where the objective is to obtain the most efficient aerodynamic shape, subject to structural constraints that account for the morphing skin behavior and the presence of the wing-box. The skin of the adaptive structure plays an important role in defining the whole morphing solution, and considering its structural behavior from the beginning helps in finding feasible structural solutions at the subsequent stages. The shape optimization performed during the first level is a single objective optimization that can be repeated several times to collect the set of target shapes and associated external design loads. The number of repetitions is M and determines the number of shape-adaptable designs considered in the MOOP of Equation (4). The multiobjective GA performed during the second level solves the MOOP by combining the M shape-adaptable designs and N structure designs.

The aerodynamic shape requires a suitable parametric representation to be described and modified. The approach adopted here is the compact Class/Shape function Transformation (CST) technique for the wing geometry representation, proposed by Kulfan in [33] and extended by PoliMi to the three-dimensional representation of a morphing wing equipped with continuous control surfaces. This fully analytical description provides several advantages, including a reduced number of parameters and a straightforward estimation of the structural strain on the morphing skin. Different aerodynamic solvers are coupled with the CST, and the resulting automatized process is nested in the overall design procedure. The aerodynamic module is used to estimate the aerodynamics performances at various conditions of the flight envelope and to provide the aerodynamics loading distribution that results from the critical design manoeuvres.

The general mathematical expression that represents the wing geometry is defined as follows,

$$z(x,y) = \zeta(\psi,\eta) \cdot c(\eta) \tag{5}$$

where $x = \psi \cdot c(\eta) + x_{LE}(\eta)$ and $y = \eta \cdot b/2$ are the dimensional coordinates defined with respect to the wing span b and the distribution of the local chord $c(\eta)$, and ψ and η are the corresponding non–dimensional coordinates, while $x_{LE}(\eta)$ is the leading edge position in the x direction along the wing span. The upper and lower non-dimensional surfaces are described as follows,

$$\zeta(\psi, \eta) = C_{N2}^{N1}(\psi)\, \mathbf{Sy}_{(\mathbf{m},\mathbf{m})}(\eta) \cdot \mathbf{A}_{(\mathbf{m},\mathbf{n})} \cdot \mathbf{Sx}_{(\mathbf{n},\mathbf{n})}(\psi) + \psi\zeta_{TE}(\eta) + (1-\psi)\zeta_{LE}(\eta) \tag{6}$$

where $C_{N2}^{N1}(\psi) \triangleq \psi^{N1} \cdot (1-\psi)^{N2}$ is the nonlinear Class function that mathematically defines a variety of basic general shapes. $\zeta_{TE} = Z_{TE}/c$ and $\zeta_{LE} = Z_{LE}/c$ are the non-dimensional vertical trailing and leading edge position, respectively. The square matrix $\mathbf{Sy}_{(\mathbf{m},\mathbf{m})}(\eta)$ contains the Bernstein polynomial components of order m which define the unit spanwise shape function; the square matrix $\mathbf{Sx}_{(\mathbf{n},\mathbf{n})}(\psi)$ contains the Bernstein polynomial components of order n which define the unit chordwise shape function. The rectangular matrix $\mathbf{A}_{(\mathbf{m},\mathbf{n})}$ contains the extra coefficients acting in a spanwise and chordwise direction, and allows to compute the two-dimensional shape function $\mathbf{S}(\psi, \eta) = \mathbf{Sy}_{(\mathbf{m},\mathbf{m})}(\eta) \cdot \mathbf{A}_{(\mathbf{m},\mathbf{n})} \cdot \mathbf{Sx}_{(\mathbf{n},\mathbf{n})}(\psi)$. Considering the matrix $\mathbf{A}_{(\mathbf{m},\mathbf{n})}$, each row defines a component airfoil, and the first and last rows contain the extra coefficients of the two airfoils placed at the tips of each wing sub-element. The first and last columns are related to the leading and trailing edge boundary conditions and can be used to define the spanwise deflection law. When the parameterization technique is used to introduce the morphing deformations, the matrix can be partitioned into three sub-matrices: the first and last portions are related to morphing the leading and trailing edge, respectively, while the middle one is related to the wing-box shape. In this case of morphing, the extra coefficients acting on the leading and trailing edge represent the optimization variables, while the other extra coefficients can be evaluated by a least-squares fitting that can meet the constraints related to the 3D wing-box volume. The mathematical formulation of this implicit constraint is similar to the parametric identification described in [34], but it is extended to the three-dimensional domain. Two different shapes of a morphing trailing edge installed on the GRA wing have been generated while considering a chordwise rear spar position equal to 80% and two different vertical trailing edge position laws reported in Figure 5. The corresponding shapes are shown in Figure 6 where the wing representation was divided into three sub-elements, which were naturally defined by two kinks.

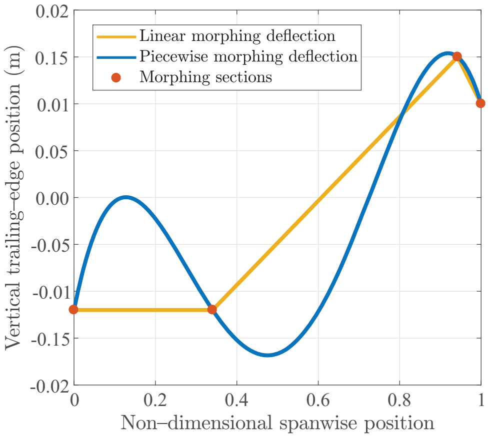

Figure 5. Vertical trailing-edge position parameter.

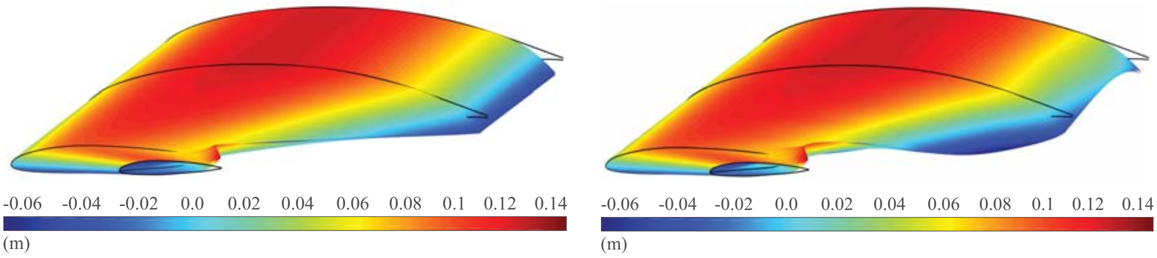

(**a**) (**b**)

Figure 6. Parametric shapes representing the GRA wing geometry equipped with a morphing trailing edge device: colors indicate the values of the vertical position function $z(x, y)$ obtained by linear (**a**) and piecewise (**b**) interpolation of four morphing trailing edge sections in span direction; the reference system is the leading edge of the root airfoil.

This first level of optimization aims at defining the best wing shape changes that satisfy specific mission requirements. When the CST is used within the aero-structural optimization loop, the aerodynamic optimality can concern the efficiency with respect to reducing the aircraft's fuel consumption, or it can concern an improvement of an arbitrary performance index I_{aero} over a wide range of different flight conditions. The optimal morphing shape is found according to the structural constraints that limit the structural response of the skin. A Constant Cross section Length (CCL) strategy is adopted to maintain a zero value for the axial strain and to limit the bending stress. The structural model of the skin is not based on the finite element method, but it is embedded into the CST formulation and exploits the capability to analytically describe the shape changes due to the morphing. Due to these constraints, in addition to an implicit constraint on the wing-box volume, aerodynamic analyses are performed only on feasible morphing shapes. A typical aerodynamic shape optimization problem, including morphing skin structural limitations, can be written as follows,

$$\min \mid \max \; I_{aero} \tag{7}$$

such that

$$\begin{aligned} \mathbf{T}^T_{m\cdot(n-r)}\mathbf{T}_{m\cdot(n-r)}\mathbf{a}^T &= \mathbf{T}^T_{m\cdot(n-r)}\mathbf{f} \\ \Delta\psi_{wing-box}(\eta) &\equiv (\psi_{fs}(\eta),\, \psi_{rs}(\eta)) \\ \mid \Delta A \mid &\leq k_a \cdot \; A_u \\ \mid \Delta L_{skin} \mid &= 0. \\ \max\,(\Delta\kappa_{skin}) &\leq \overline{\Delta\kappa} \end{aligned}$$

According to the optimization algorithm described in [34], the first term represents the implicit wing-box constraint. It acts on the three-dimensional wing-box region, which is delimited by the front and rear spar positions, and it is described by $l+1$ pairwise distinct coordinates coming from the CAD model of the undeformed wing. $\mathbf{T}_{m\cdot(n-r)}$ represents the $(l+1) \times m \cdot (n-r)$ *reduced CST-Vandermonde matrix*, where r is the number of perturbed coefficients, and $\mathbf{f}$ is the corresponding $(l+1)$ vector. The unique solution of this linear system is equivalent to solving, in the least squares sense, the over-determined system that allows us to compute the $m \cdot (n-r)$ extra coefficients of the matrix $\mathbf{A}_{(\mathbf{m},\mathbf{n})}$, reorganized in the vector $\mathbf{a}$. The $l+1$ pairwise distinct real points are given and placed along the wing-box region, which must be kept undeformed. The r extra coefficients for each row of the matrix $\mathbf{A}_{(\mathbf{m},\mathbf{n})}$ are the optimization variables that affect only the domain outside the wing-box region. The second constraint represents the wing-box extension defined by the non-dimensional front spar position $\psi_{fs}(\eta)$ and rear spar positions $\psi_{rs}(\eta)$. The inflatable term k_a allows us to limit the internal area variation ΔA, with respect to the internal area of the undeformed wing shape A_u, and it is introduced to avoid the generation of unrealistic morphing shapes. The main structural constraint for the skin is to keep its skin length L_{skin} constant to avoid axial stress. The last constraint is used to limit the maximum curvature variation $\Delta\kappa_{skin}$ computed between the undeformed shape and the morphing shape. This strategy allows us to control the maximum bending strain ε_{bend} according to the material properties of the skin, as follows,

$$\varepsilon_{bend} = \frac{t}{2}\left(\Delta\kappa_{skin}(l)\right) \tag{8}$$

where t is the skin thickness, and l is the arc length function defined in the chordwise direction. It is important to note that this optimization problem does not depend on the material of the compliant structure that is designed in the next level. The results of the first level are all target shapes, and they correspond to aerodynamic loads, which allow us to formulate the multiobjective problem 4.

3.2. Second Level

The second level optimization inherits a set of aerodynamic morphing shapes that arise from the morphing shape optimization problem described in Section 3.1. The number of aerodynamic shapes is equal to the number of multiple load conditions and defines a corresponding set of design load cases. Given these shapes and the corresponding external loads, the second level aims at designing a suitable internal compliant structure that can match, properly actuated and under external loads, the desired morphing shapes. According to the shape-adaptable design problem (3), aerodynamic shapes represent multiple objective functions at this level. Each objective function is associated with the corresponding design loads, which increases the total number of objective functions. The compliant structure must be able to satisfy the kinematic and structural requirements, for each pair of shapes and loads. This problem is a typical multiobjective design problem that can be efficiently incorporated into an EA, which can find multiple optimal solutions in one single simulation run due to its population approach. In the case of adaptive wing structures, the multiobjective design problem (4) has the shape-adaptable problems combined with the structure design problems (2). The proposed approach is based on a dedicated Multiobjective Genetic Algorithm (MOGA) coupled with a Load Path Representation.

The load path representation is a design parameterization of the stiffness tensor, which makes use of load paths to represent different structural topologies, cross-sectional beam areas, and the positions of the internal points of interest for the shape problem. The load path representation is described in [23], where it is coupled with a Single-Objective Genetic Algorithm (SOGA) to solve the kinematic design, under a single load condition. This method has been further developed and extended to MOGAs, as described in this article. The same approach can be used for the synthesis of SISO compliant mechanisms [35], and for the design of SIMO compliant structures that aim at shape control. The load path representation method is coupled with a nonlinear analysis solver, and each set of load paths is transformed into a sequence of Finite Volume Beams [36]. Nonlinear analyses are performed to correctly describe the behavior of compliant structures subject to large displacements. The proposed method combines different types of techniques: sizing, geometry, and topology optimization. In the sizing optimization, the cross-sectional areas of each beam of each load path are considered to be design variables; in the geometry optimization, the design variables are the coordinates of the internal points that define the load path sequence and the intersection between the different load paths; in the topology optimization, the connectivity of the load paths is to be determined. In the second level proposed here, all of the three optimization problems are considered simultaneously, and the load path representation is essential to unifying all three optimizations. A solution represented in the GA population is a mixed vector of binary, integer and real numbers within specified ranges. The presence or absence of a load path in the compliant structure is determined by the binary variables that allows us to obtain different topologies.

The approach used to solve the MOGA problem applied for our purposes is the so-called Elitist Non-Dominated Sorting Genetic Algorithm (NSGA-II) [24]. In NSGA-II, the offspring population is combined with the parent population, from which it is created, to form a population of size

$2N$, where N is the initial population size. Instead of finding the non-dominated front only, the two populations are considered together, and a non-dominated sorting is used to rank the entire population. This approach requires more computational effort, but it allows a global non-dominated check among offspring and parent solutions. The diversity inside the population is introduced by using the crowding comparison procedure, which is used with the tournament selection and during the population reduction phase. As solutions compete with their crowding distances, no extra niching parameter is required. The NSGA-II can find a number of trade-off solutions between the different objectives in one single simulation run. The most important and useful aspect from the compliant structure point of view is that the obtained non-dominated front has distinct regions with different topology solutions. Within each region, the solutions vary by having different cross-sectional areas of load-paths, while keeping the same topology. Each region has a limit in the values of the objective functions. To improve a solution beyond these limits, a different topology, and thus a different region of the Pareto front, must be explored. During the design activities, knowledge of these trade-off solutions allows us to select the most suitable design point. The Pareto front represents all of the possible and feasible internal structure solutions that can produce all of the aerodynamic shapes that the device must be able to take during the mission, under all of the external loads selected from the flight envelope.

Once a set of non-dominated solutions is obtained, some higher-level decision-making considerations are usually used to choose a preferred Pareto-optimal region. To find a preferred set of solutions, a specific material is assigned and the Pareto-optimal solutions are accepted or discarded while considering the stress constraints inside the compliant structure. For this reason, the minimization of the stress computed in the internal structure can be added to the multiple objective functions to have an automatically non-dominated sorting of the solutions with respect to the stress values. For the same reason, different types of dynamic requirements can also be used to define the objective functions. The designer selects the preferred Pareto-optimal region directly from the Pareto Front, while accounting for the manufacturing requirements, such as the local thickness changes along the skin, the distance between load paths to avoid contacts inside the mechanism, and the angle between each load path and the skin. The angle determines the connection between load paths and skin, which is realized by the use of stiffeners. The stiffeners contribute to reinforce the skin in span direction and are usually manufactured together with the skin, using two curing stages. These criteria are not included in the optimization problem of the second level, but drive the choice of the Pareto-optimal region and can be transformed into optimization constraints during the third level. However, the most important manufacturing detail concerns the fillets inside the rib model, around the intersections between different load paths. This last criterion is made effective by anticipating the CAD model generation that is included in the fourth level. After the preferred Pareto-optimal region is chosen, the design point that corresponds to the preferred solution is selected by identifying a decision-making criterion, such as the so-called marginal rate of substitution approach. It is based on considering the amount of improvement in one objective function while accepting a unit decrement in the other objective functions. The solution that has the maximum marginal rate, among the Pareto-optimal solutions of a specific region, is chosen by this criterion. At the end of the process, the designer selects the design point directly from the Pareto Front, while accounting for the manufacturing requirements, such as the local thickness changes and the angle between each load path and the skin, which are not included in the optimization problem. This last criterion is made effective by anticipating the CAD model generation that is included in the fourth level.

The second level generates conceptual single-part mechanisms and helps to create a 2D representation of a compliant structure that bends for functionality. The multiobjective optimization comes up with the closest topology that it can find to meet the input and output requirements. The algorithm finds the optimal compliant structure for a selected rib along the wing span, which will be extended to a complete 3D space in the next levels. An example is reported in Figures S1 and S2, where one morphing trailing edge has been designed while considering two aerodynamic shapes and the corresponding aerodynamic loads: the same compliant structure must be able to deform itself to match one optimal aerodynamic shape for the upward deflection and one optimal aerodynamic shape for the downward deflection, respectively. These aerodynamic shapes are directly extracted from the three-dimensional morphing shape of Figure 6.

It is important to underline that the stress requirements are optional at this stage: they can be included in the MOGA as constraint functions or as objective functions, or they can be considered at the end of the optimization by discarding from the Pareto front all of the solutions that are subjected to a maximum stress that is higher than a chosen threshold. Nevertheless, the presence of a stress limitation does not invalidate the material-independent character of the topology solution from the genetic optimization. Indeed, the demand of a stress restriction can be thought to avoid stress peaks and to uniformly distribute the stress inside the entire structure, regardless of the choice of the adopted material. The actual material to be assigned to the compliant structure is considered in the third and fourth levels, where the corresponding admissible stress values become an effective constraint function inside the optimization.

3.3. Third Level

Topology optimization assumes a fundamental role in the definition of the compliant structural configuration that can supply the desired deformation. Genetic algorithms represent a global method that can explore a large portion of the space of solutions for defining a suitable topology. However, it must be followed by a local optimization to determine a more accurate sizing of the mechanism and to refine the optimal solution selected on the Pareto front. The third level consists of a sizing and geometric optimization based on a constrained nonlinear optimization. A Sequential Quadratic Programming (SQP) approach is chosen at this stage.

The scalar objective function is defined by choosing it among all of the objective functions considered in the second level. All of the other objective functions become constraint functions because they must at least preserve the same value that they assume at the end of the second level. Stress constraint functions are added to account for the mechanical limitations of the material that the compliant structure is made of. To correctly evaluate the stress, the topology solution is specialized while considering the actual material and manufacturing details [37]. Geometry and sizing constraint functions can be added to account for the manufacturing requirements, as described in Section 3.2. The objective and constraint functions are computed under the loads computed during the first level. Optimization variables are the same as in the previous level except for the topological variables that are not present.

Objective and constraint functions are evaluated as a result of the finite element analyses performed by Abaqus. A medium/high-fidelity model obtained by a constant-section extrusion is used at this level, and a more accurate finite element model of the skin, also in terms of material behavior, is introduced and allows the modeling of the stiffeners. The length of the skin in the span-wise direction is equal to the actual rib pitch, and a model is made of a single rib in the middle or a pair of ribs at the ends of this portion. The goal is to not exceed the elastic properties of the actual material while considering a model with higher fidelity than the model used at the previous level. The generation of the model is automatic and exploits the Abaqus Scripting Interface (API), which is an extension of the Python object-oriented programming language [38]. Since large deformations are expected, static nonlinear analyses are used.

This level can be repeated for different sections along the wing span, or to change the Pareto-optimal solution if considering actual materials or manufacturing details or if a more accurate model makes the results too much worse. From this point of view, the choice of the Pareto-optimal solution and the third level can represent an iterative design loop.

3.4. Fourth Level

At the end of the previous step, the numerical design phase can be considered to be finished, as an optimized model has been obtained such that it well satisfies the requirements in terms of the shape quality of the deformation and, at the same time, it does not violate structural limitations. Last step, but not the least important, allows us to verify the structural performance of the complete active adaptive wing device, to simulate the three-dimensional and time-varying nonlinear elasticity and the structural dynamics. The starting point of the fourth level is the three-dimensional CST representation of the external wing shape and the set of optimal compliant structure solutions that are computed for different sections along the wing span. To generate the finite element model of the entire morphing device to be installed on the wing, an automatic interface between the CST technique and computer-aided engineering software, including Abaqus and CATIA, has been developed. This level enables the manual creation of manufacturing details, actuation kinematics, and connections between different parts of the structure, and it provides greater capabilities for modification. Moreover, it is possible to adjust the thickness of each compliant rib to meet the forces that are needed. Modeling of all of these details allows for a more realistic estimation of the stress distribution inside the structure and three-dimensional shape quality verification. The structural solution shown as an example in Figures S1 and S2 is used to generate the finite element model of a complete compliant trailing edge device. It can produce a spanwise twist deformation, as shown in Figure S3, exploiting the capability of the designed compliant structure to achieve both upward and downward deflections.

A CAD model of the compliant mechanism can also be created starting from the automatic generation of different plane sketches along the span. They exhibit the actual internal point positions, the load path thicknesses and suitable fillets that link the lines at the intersection of the optimal solution. Starting from the CAD model of a compliant rib, the corresponding full-solid finite element model can be generated and used to optimize the shape of the fillets. This structural shape optimization allows to reduce the stress peaks inside the compliant structure, by increasing the fatigue life and the reliability of the compliant device.

The availability of the complete device model enables the evaluation of other three-dimensional effects that are essential for the integration of the device with the wing. The complete model can be connected to a wing-box finite element model that reproduces the correct flexibility of the wing. In this way, the interaction between the adaptive structure and the wing-box can be evaluated while considering the static aeroelastic effects of the entire wing, for each flight condition. In the following application, the effects of the wing-box deformation on the shape quality of the actuated device are evaluated.

4. Morphing Leading Edge Application

In the framework of the EU-funded Clean Sky 2 REG-IADP AG2 project, the Reference Aircraft (RA) is a 90 pax, twin prop Green Regional Aircraft (GRA). The role of an innovative aircraft development platform dedicated to regional aircraft is to validate the integration of new technologies at a high level of maturity into future aircraft. European regional aircraft attempt to be highly competitive in terms of performance by installing advanced devices on the reference wing, which is a Natural Laminar Flow (NLF) wing and optimized by ONERA inside the AirGreen2 (AG2) consortium. The CAD model of the RA is shown in Figure 7. Different morphing concepts are considered such as morphing droop nose, morphing flap, and a morphing winglet. PoliMi is in charge of several activities including the development of active systems for load control and alleviation, and the design and integration of a fully compliant structure for the morphing leading edge.

The morphing leading edge is a full-span and 16% chordwise configuration that is composed of two regions: inboard and outboard separated by the nacelle. The main goal is to delay the wing stall in take-off and landing conditions, without affecting the NLF wing aerodynamic performances of the reference configuration. This target must be obtained by keeping the skin surface seamless and smoothed to avoid producing any anticipated loss of laminarity, and this requirement forced the adoption of an innovative solution to avoid the adoption of a classical slat. The requested $C_{L,max}$ enhancements are equal to 2.4% and 1.7%, considering both the flap and leading edge morphing effects in take-off and landing, respectively.

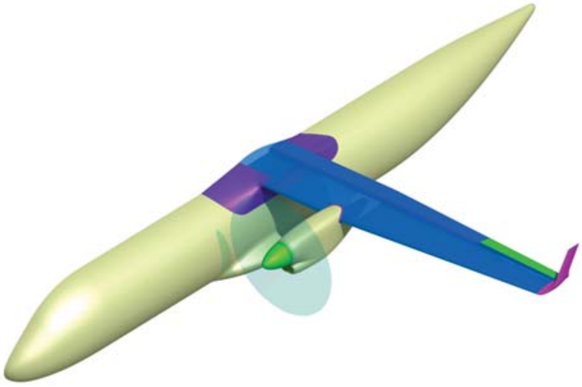

Figure 7. CAD surfaces of the reference aircraft.

Starting from these general requirements, the design procedure described in Section 3 has been applied. The approach here is adopted for the design of the morphing leading edge and is based on a fully compliant structure, composed by a complete skin and by a series of internal compliant ribs, which once actuated, force the skin to assume the target shape optimized for aerodynamic purposes. The definition of compliant skin for a morphing device is one of the most challenging design phases, while the main difficulty in the design internal compliant structure of a morphing leading edge, compared with a trailing edge, is the different chord extension. This approach involves a higher level of internal stresses to achieve the desired deflection. Moreover, in the case of the morphing leading edge, the certification also requires bird impact compliance, but this part of the work is not described in this article because the major aim of this application is the validation of the optimization design procedure.

The following sections describe the activities conducted to apply the different levels of the proposed procedure, with a special focus on the outboard leading edge only, as the same approach has been adopted on the inboard region.

5. Results

The four-level optimization procedure is applied to the design of the morphing droop nose to be installed on the GRA.

Concerning the set of load cases to be considered in the design of the morphing leading edge, the starting point has been the critical loads suggested for conventional leading edge slats in [8]. Droop nose high-lift devices are usually critical for positive loads at the upper left-hand corner of the V-n diagram and for negative loads at the right-hand corner. The critical positive load occurs at the designer manoeuvre load factor of $n_Z = 2.0$ if the wing is in the flaps-down configuration, and at the maximum lift coefficient if the flap is not deployed. The critical negative load acts on the leading edge at $n_Z = 0$, at the placard speed V_F, when the wing is in a flaps-down configuration. Moreover, the authors of [8] warn that the leading edge slats could be critical for bending induced by the wing flexibility on the slat structure. This approach is combined with the external aerodynamic pressure acting on the leading edge skin, and the actuators react. The same set of critical loads is considered by the multilevel procedure for the design of the morphing leading and the effects of the wing deformation, which are verified in the fourth level.

During the first two levels, independent-material solutions are obtained in terms of optimal aerodynamic shapes and 2D topology solution for the internal compliant ribs. During the next two levels, actual materials are assigned and compliant ribs are packed together with the skin into a single fully compliant 3D model used for final refinement and verification. The final configuration is based on a solution that is reinforced with a limited number of stiffeners, which are not considered in the first two levels. Stiffeners are used to reinforce the skin and minimize the anticlastic deformations and to introduce physical connections between the skin and the compliant ribs. The skin is composed of an anti-erosion layer (AEL) and a skin structural layer (SSL) made of composite material, while the third level of the procedure is applied twice, and two different materials are considered for the design of the compliant ribs: aluminium alloy and NiTiNOL (Nickel Titanium Naval Ordnance Laboratory). NiTiNOL is used in a passive way, by exploiting its superelastic behavior, instead of using the shape memory effect, to limit the stress level in the internal compliant structure.

Although the design of the morphing leading edge started from scratch, some design parameters have been defined, such as the rib pitch, equal to 260 mm, and the front spar position, which depends on the wing layout. Moreover, assuming a constant rib thickness in a span direction of 35 mm, the chord-wise thickness distribution is defined by the MOGA during the second level of optimization.

5.1. First Level

Considering the aerodynamic interaction between the morphing droop nose and the flap is the only way to catch the actual best performances related to the use of the proposed advanced high-lift device. Therefore, the shape optimization adopted at the first level of the proposed procedure is applied to the NLF wing of the reference regional aircraft, while considering a flap deflection of 35 deg in the landing configuration. The optimization problem is based on Formula (7), where I_{aero} aims at producing the maximum droop deflection along the wing span that can achieve the maximum stall angle, for a single low-speed condition. The morphing droop nose acts by extending the baseline $C_L(\alpha)$ curve to reduce the flap deflection. As there is no C_L variation due to the droop nose for angles of attack before the stall, maximizing the stall angle is equivalent to maximizing the $C_{L,max}$. Two wing sub-elements—one for the inboard and one for the outboard region—are considered. Each wing sub-element is represented by a Bernstein polynomial of the order of $n = 10$ (BPO10) for the unit chordwise shape function and a Bernstein polynomial of the order of $m = 5$ (BPO5) for the unit spanwise shape function. This approach means that the size of the two extra coefficient matrices is 5×10. The first $r = 2$ columns of the matrix contain the extra coefficients that can be perturbed by the shape optimization, and they represent the optimization variables. However, according to the initial design requirements, the optimization constraints include a linear deflection law of the morphing droop nose in the spanwise direction, along both the inboard and outboard regions. Therefore, the extra coefficients of each of the first two columns are linearly dependent, and thus only the first two coefficients of the first and last row are used as optimization variables for each sub-element. Moreover, the airfoil shape at the kink section must be the same for the inboard and outboard sub-element, and thus, the total number of optimization variables is 12, 6 for the upper surface and 6 for the lower surface. Additional optimization constraints include the skin length and the maximum skin curvature. The skin length is set to be constant to avoid axial strains into the skin, while the maximum skin curvature is set to avoid variation above $20\,\frac{1}{m}$. According to the minimum thickness of a composite skin, this value corresponds to normal strains due to bending that do not exceed 1%. They depend only on geometrical considerations, instead of axial and bending stresses, which depend on the material properties and skin thicknesses, which are unknown at this stage.

All of the details related to the aerodynamic solver, its integration with the optimization process and how the shape design was conducted can be found in [39]. The optimal morphing shape for both the landing and take-off conditions has been defined. Two-dimensional Bernstein polynomial shape functions for both undeformed and maximum droop nose deflection configurations are reported in Figure 8. The corresponding spanwise vertical leading edge position is reported Figure 9 together with the corresponding skin curvature variation that satisfies the structural constraints. The maximum droop deflection is constant in the inboard region, while it linearly decreases from $Z_{LE} = -0.13\,m$ to $Z_{LE} = 0\,deg$ in the outboard region.

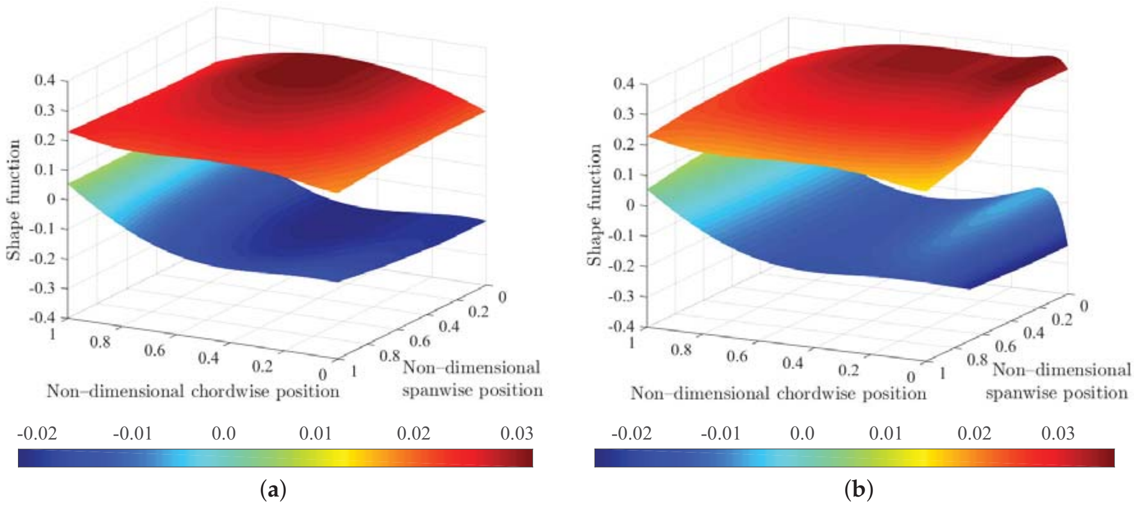

(**a**) (**b**)

Figure 8. Non-dimensional shape functions of undeformed (**a**) and morphing (**b**) wing geometries: colors indicate the values of the function $\mathbf{S}(\psi, \eta)$ in the non-dimensional square domain.

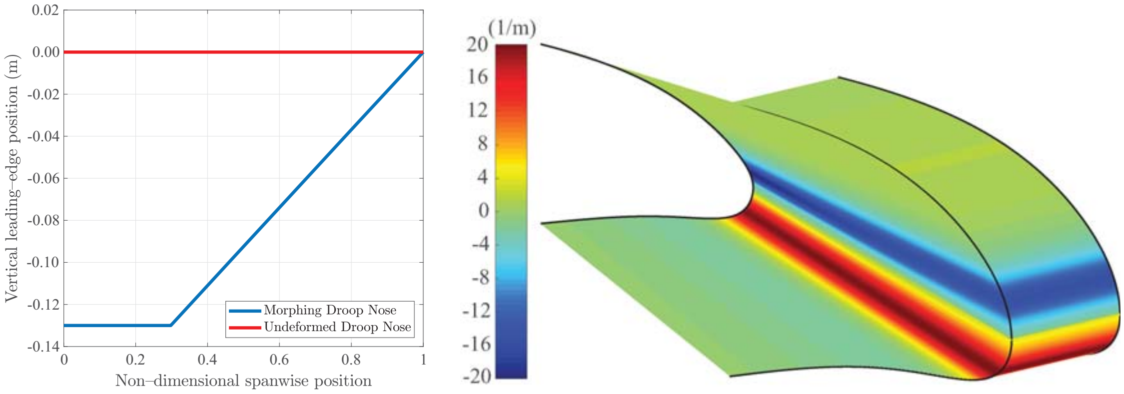

(**a**) (**b**)

Figure 9. Vertical leading-edge position parameter (**a**), and corresponding morphing Class/Shape function Transformation (CST) shape and skin curvature variation (**b**).

The CAD model of the optimal shape that reproduces the maximum droop nose deflection has been attached to the NLF wing and used to generate a structured aerodynamic mesh. The complete surface model is shown in Figure 10. Three-dimensional RANS computations have been conducted in fully turbulent mode, and the results, in terms of the assessment of the aerodynamic performances, can be found in [39]. In comparing aerodynamic coefficients for both take-off and landing configurations, with or without the morphing droop nose device, it has been observed that the use of a morphing leading-edge is necessary to respect the performance level required for the landing conditions, in terms of the maximum lift coefficient. The use of the morphing leading-edge increases the stall angle by approximately $\Delta\alpha(C_{L,max}) = +5deg$ for the landing condition. The performance improvement, in terms of the lift coefficient, is $\Delta C_{L,max} = +15\%$, while the drag coefficient variation ΔC_D is negligible. In take-off conditions, the use of the morphing leading-edge increases significantly the stall margin $\Delta\alpha(C_{L,max}) = +2.5deg$, and it leads to an increment of $\Delta C_{L,max} = +10\%$ and a constant decrease of $\Delta C_D = -5\%$ on the complete C_L range.

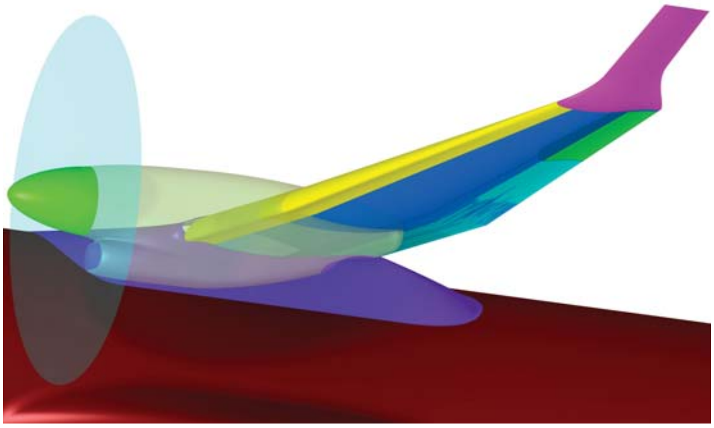

Figure 10. CAD surfaces of the Reference Aircraft (RA) wing with an optimal morphing droop nose.

The optimal three-dimensional shapes, selected after the aerodynamic assessment, are used as target shapes for the definition of the objective functions coupled with the estimation of the set of critical load cases for the second level of optimization. Moreover, they permit the definition of the optimal actuation points along the skin [23]. The mapping between the target and undeformed shapes allows the definition of the optimal actuation points which represent the best arc-length positions along the skin where the compliant structure can be connected, for the purpose of introducing the shape changes in the most efficient way. This approach also enabled a preliminary study of the morphing skin structural configuration, before the internal structure is defined, using the same points to introduce the enforced displacements that correspond to the shape changes defined by the target shapes. This step has allowed us to define the most suitable lamination sequence to be assigned to the skin material, which will be introduced in the third level of optimization.

The set of critical load cases, used by the second level of optimization, are shown in Figure 11 in terms of the pressure distribution acting on the wing. The first load case refers to the wing shape without a morphing leading edge, with an angle of attack of α = 18 deg and a dynamic pressure of q_D = 2561 Pa, which correspond to the landing conditions at sea level. The second load case refers to the maximum droop nose deflection shape, with an angle of attack of α = 0 deg and a dynamic pressure of q_D = 5000 Pa, which correspond to the Placard speed V_F at sea level.

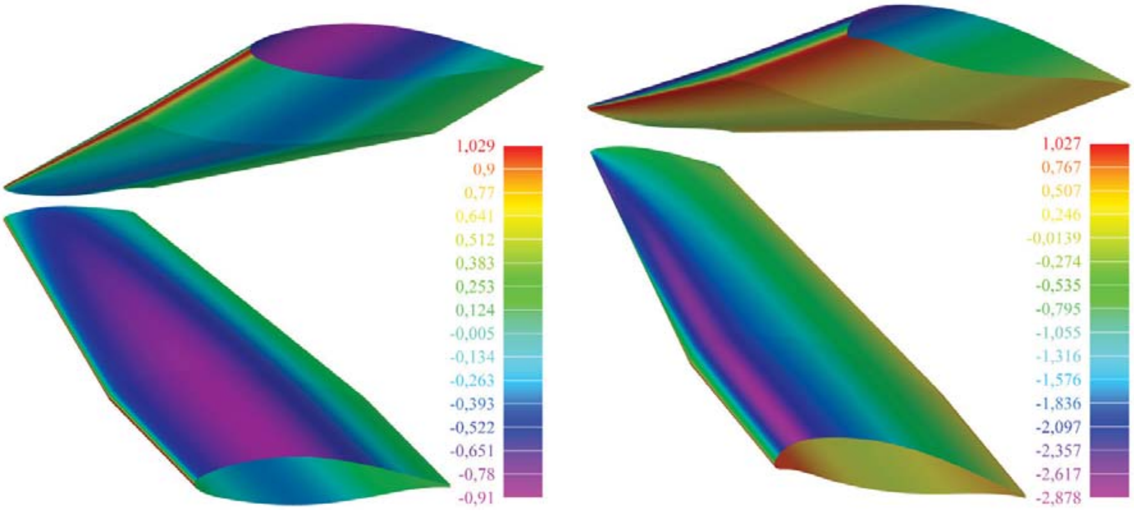

(**a**) (**b**)

Figure 11. Pressure coefficient C_p that correspond to undeformed shapes and placard speed conditions (**a**) and to morphing shapes and landing conditions (**b**).

5.2. Second Level

The set of load cases that correspond to the optimal aerodynamic shapes and to the most critical flight conditions defined in the previous section are concurrently considered for the design of the adaptive leading edge. This design is performed by means of multiobjective optimization, based on the load path representation coupled with the dedicated genetic algorithm, described in Section 3.2. It works to define the two-dimensional topology configuration of the internal compliant ribs and a preliminary sizing of the skin and ribs. The combination of the following three objective functions is considered.

1. Structure design: minimizing the Strain Energy (SE) to preserve the NLF wing shape, as reported in Section 2.2. The actuation point is kept fixed, and the compliant structure is subject to the aerodynamic loads that correspond to the Placard speed at sea level (Mach = 0.52).
2. Shape-adaptable design: minimizing the Least Square Error (LSE) between the maximum droop nose deflection shape and the leading edge deformation, as reported in Section 2.3. The compliant structure is actuated under the aerodynamic loads that correspond to the landing flight condition at $\alpha = 18$ deg and sea level (Mach = 0.197).
3. Minimizing the maximum value of the total stress in the compliant structure, when it is actuated, under the same aerodynamic loads considered in the second objective function.

Stress values for the computation of the third objective function are recovered only on the compliant rib model. An equivalent structural constraint for the skin is already embedded into the definition of the target shape, which is obtained by imposing a limitation on the length and curvature variation during the first level of optimization. In this way if the second objective function converges, the compliant structure solution implicitly satisfies the skin structural constraints inside the skin.

The finite element model is characterized by two clamps at the upper and lower skin, which represent the connection points with the front spar (numbers 2 and 3), while a stroke, predetermined by the actuation kinematics, pushes the compliant rib in the direction shown in Figure 12, acting on point number 1. A total of nine internal points (numbered from 24 to 32) are collocated in the user-defined domain to automatically define the initial load paths network. The maximum load path length, which defines the maximum number of edges that form a single load path, is set to be equal to 3, and the thickness of each edge is free to vary during the optimization. A total of nine active output points (numbered 4 to 12) is used for transferring the actuation load from the compliant rib to the contour skin. They define the integer variables that are used by the GA to change the load path destinations. The thickness of the skin is free to vary interdependently on 10 separate regions during the optimization process. Additional points are introduced along the contour skin to improve the resolution of the LSE and to better interpolate the aerodynamic loads. The aerodynamic loads that correspond to each load case are obtained by slicing and interpolating the aerodynamic pressure field, shown in Figure 11, with a plane parallel to the ribs.

The initial population contains 500 individuals, while the number of genetic variables is equal to 200. The entire load path network is shown in Figure 12. According to the maximum load path length and the number of characteristic points, the number of binary variables is 29, the number of integer variables is 56, and the number of real variables is 115. During the process, the load path cross-sectional thickness was free to vary between 1 mm and 6 mm, and the actuator stroke was set to 3.6 cm with an angle of 5 deg downward. Thickness values of the 10 skin regions are included in the design variables. The GA was left free to run for a maximum of 700 generations. After 510 iterations, the Pareto front shown in Figure 13 was invoked, which made it easier to identify the best design trade-off between the shape-adaptable, structure and stress objective functions. The number of solutions included in the Pareto front is equal to 175. To select the preferred Pareto-optimal region, different types of considerations were accounted for, such as a good compromise between the conflicting requirements and expected manufacturing details. One of the criteria that drove the choice was the presence of a load path connected to the upper skin in the solution. Following these decision-making considerations, the red circled region in Figure 13 was selected. Considering a fictitious Young's modulus E = 70 GPa, the point highlighted with red color in the same figure was selected considering a maximum stress value inside the compliant structure. The structural configuration of the selected solution is shown in Figure 14, and it represents the starting point for the last two levels of optimization.

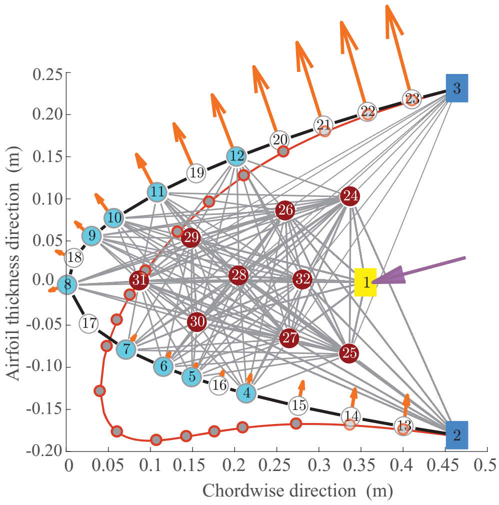

Figure 12. Initial population and load path model set-up: load path network (grey), active output points (cyan), deactivated output points (white) to improve the distribution of the external loads (orange arrows), internal structure points (red), constraint points (blue), input actuation point (yellow), and stroke actuation (purple arrow). Target points are placed along the target (red) curve, at the same arclength as the output points.

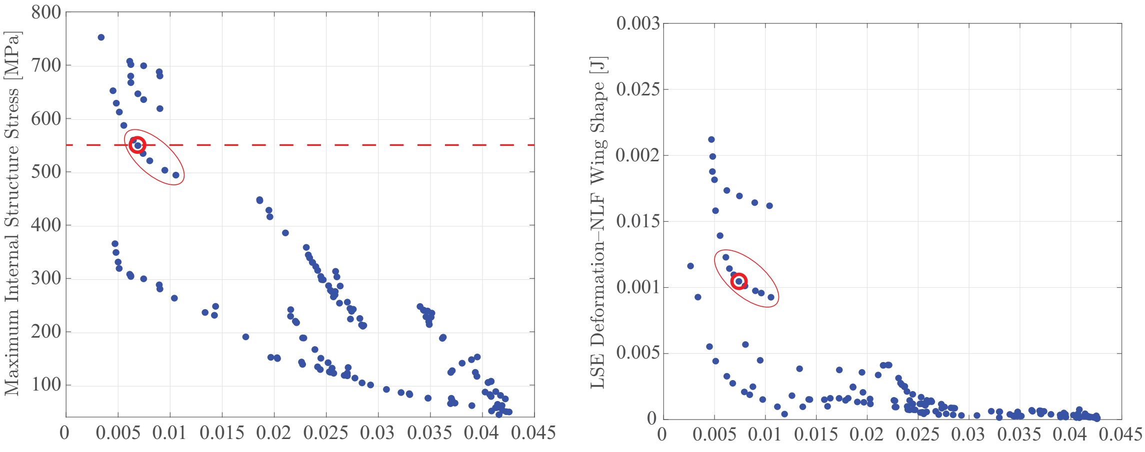

(**a**) (**b**)

Figure 13. Pareto front, selected Pareto-optimal region, and selected design point: shape-adaptable design vs. stress minimization (**a**) and shape-adaptable design vs. structure design (**b**).

The choice of accepting such a high level of stress equal to 550 MPa, is dictated by the need of achieving high droop nose deflections, which are required to be close to the morphing target shape, at the same time, preserving the NLF wing shape as much as possible. Obviously, it is unthinkable to presume the availability of an aluminum alloy with such a yield strength. This aspect is confirmed by the maximum principal strain provided by the finite element analysis, which is equal to 0.76%, higher than the yield elongation of a typical aluminum alloy, which is 0.65%. The basic idea behind this choice is to use the next level to assign a different material that can guarantee highly recoverable strains of greater than 1%. This potentiality can be found in the superelastic behavior of NiTiNOL as an alternative to the aluminum alloy. The next level is repeated for both materials to compare the results and validate the proposed multilevel procedure.

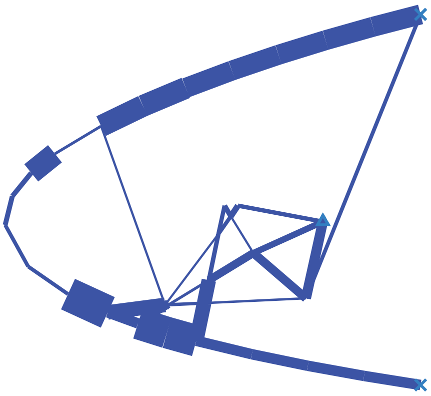

Figure 14. Representation of the optimal compliant structure configuration.

5.3. Third Level

Starting from the topology solutions that arise from the second level of optimization, a higher fidelity model than the previous two-dimensional model is generated and used inside the constrained nonlinear optimization of the third level. A local optimization, based on Sequential Quadratic Programming (SQP), is used to refine the structural solution selected on the Pareto front. The second objective function of Section 5.2 becomes the single objective function, while the other two become two nonlinear constraints in such a way that their value does not get worse than the same values accepted on the Pareto front. The optimization variables are the same variables used by the GA, except for the topology (binary) variables: the number of load paths can not change at this stage. The finite element model is automatically generated and initialized considering the values that the optimization variables assume when the design point is extracted from the Pareto front. It is a constant-section model that reproduces the behavior of the portion between the two ribs, as depicted in Figure 15. The actuation stroke is introduced by a kinematic chain that can reproduce the actual displacements.

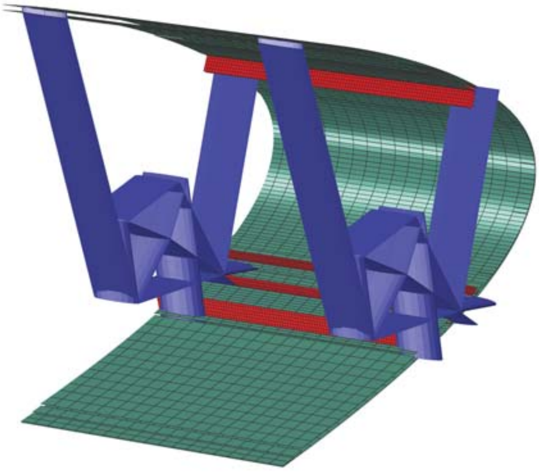

Figure 15. Finite element model used by the third level of optimization.

The actual materials are also assigned to both the skin and compliant ribs. The Skin Structural Layer (SSL) is made of Glass Fiber-Reinforced Polymer (GFRP), the mechanical properties of which are reported in Table 1. The aim of this layer is to provide a suitable stiffness in both the chord and span direction. As in the second level of optimization, the chordwise thickness distribution is determined by the optimization, but it now considers a more accurate material model. The skin structural configuration embeds 4 T shaped stiffeners, which are not considered in the first two levels;

these are used to reinforce the skin in the spanwise direction and to correctly model the connections between the compliant rib and skin. The stiffener lamination sequence is symmetrical with the thickness and is equal to the local SSL thickness. Two different stiffener geometries, for low and high curvature airfoil areas, are used.

Table 1. Fiberglass fabric mechanical properties.

Parameter	Description	Value
E_{11}	Young's modulus in x-direction	25 GPa
E_{22}	Young's modulus in y-direction	25 GPa
ν	Poisson's ratio	0.20
G	Shear modulus	4 GPa

Two optimizations are performed by first assigning the aluminum alloy and then NiTiNOL to the compliant ribs. NITiNOL is used to exploit its superelastic capabilities, which allow it to recover from very large strains upon unloading, without permanent deformations. The existence of a transformation stress plateau guarantees near constant stress over large strain intervals. To define the superelastic material model, 15 constants must be supplied if plastic deformations are not permitted, as in the aeronautical case. A simple numerical material design is conducted while accounting for a wide range of aeronautical operative temperatures, and it is described in [37]. Some material properties are borrowed from Qidwai and Lagoudas [40], and they are reported in Table 2. The transformation strain is 5%, while the elastic strain is 2%. The stress values that characterize the plateau, in terms of the start and end of the transformation loading, are σ_L^S = 441.1 MPa and σ_L^E = 511 MPa, respectively.

Table 2. Nitinol mechanical properties.

Parameter	Description	Value
E_A	Austenite Young's modulus	70 GPa
E_M	Martensite Young's modulus	30 GPa
ν	Poisson's ratio	0.3

The Young's modulus and the Poisson's coefficient for the aluminum alloy are equal to the same values considered for the NiTiNOL in the elastic part of its constitutive curve. The admissible stress value considered during the optimization for the aluminum alloy is 550 MPa, according to the same unfeasible value accepted during the selection in the Pareto front. The admissible stress value for the NiTiNOL is 500 MPa, which is just below the stress level at the end of the loading plateau. During the optimization, the load path thickness is free to vary between 1 mm and 7 mm, while the skin thickness distribution is free to vary between 0.5 mm and 7 mm. The constrained non-linear optimization converges to an optimal solution in 52 iterations when the aluminum alloy is considered. The LSE value of the optimal solution is 2.23 mm, and the maximum stress value found in the ribs is equal to 549.9 MPa, which satisfies the stress constraint. The comparison between the initial deformed shape and the optimal deformed shape is shown in Figure 16, where the stress distribution and the comparison between the deformed and target shapes are also illustrated.

The same constrained nonlinear optimization that considers NiTiNOL converges to an optimal solution in 49 iterations. The LSE of the optimal solution is 1.44 mm, while the maximum stress in the rib is 462 MPa, which corresponds to a maximum strain of 1.8%, which is in the range of the recoverable strains. The comparison between the initial deformed shape and the optimal deformed shape is shown in Figure 17, where the stress distribution and the comparison between the deformed and target shapes are also illustrated.

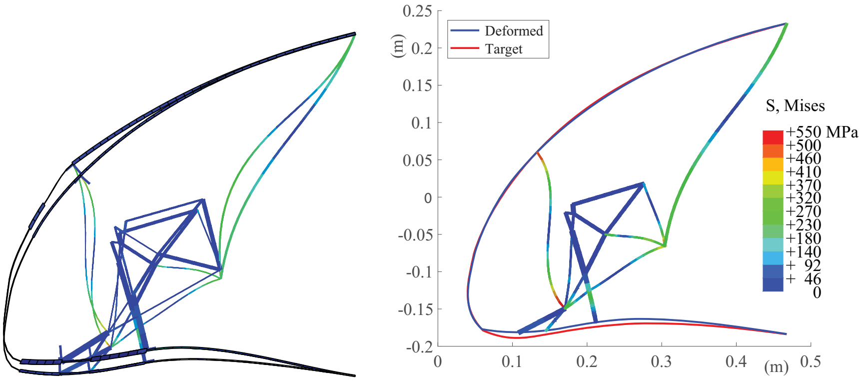

(**a**) (**b**)

Figure 16. Isotropic material: deformation of the initial and optimal solutions (**a**); Von Mises stress in the rib and comparison between the optimal deformation and the target shape (**b**).

The comparison between the aluminum- and NiTiNOL-based solutions shows that the use of different materials leads to a rearrangement of the thickness distribution inside the compliant structure to minimize the objective function. The internal point positions are also slightly changed. The comparison between the two final structural configurations and the initial one is shown in Figure 18.

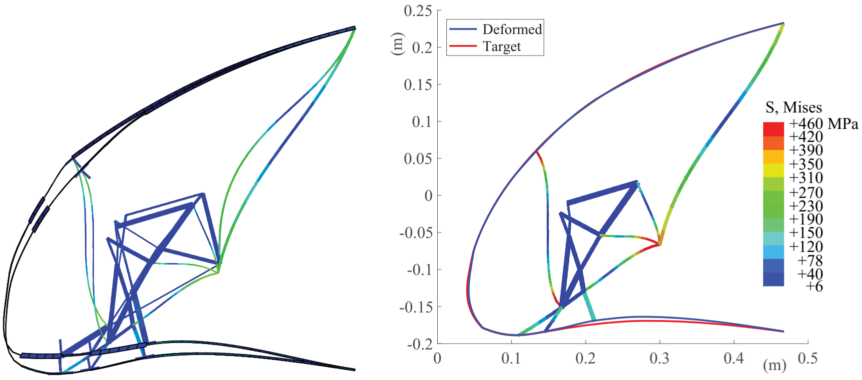

(**a**) (**b**)

Figure 17. NiTiNOL: deformation of the initial and optimal solutions (**a**); Von Mises stress in the rib and comparison between the optimal deformation and the target shape (**b**).

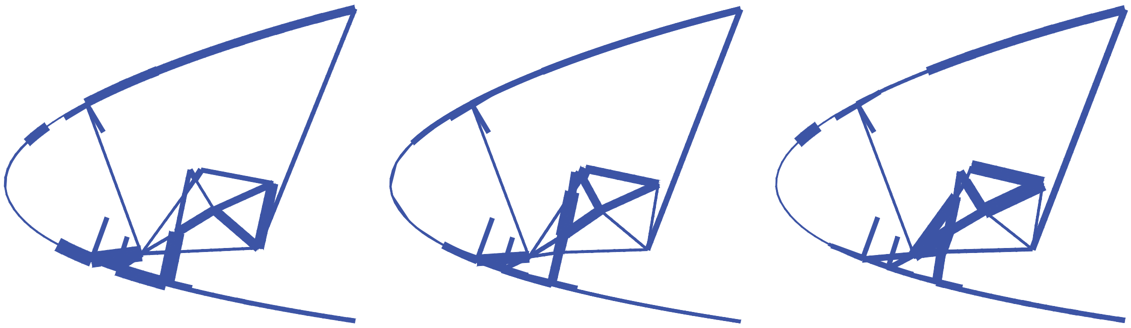

(**a**) (**b**) (**c**)

Figure 18. Solution comparison: initial solution (**a**), optimal aluminum solution (**b**), and optimal NiTiNOL solution (**c**).

The results show that the third level of optimization produces a general shape quality improvement of the *LSE* values compared not only to the initial deformed shape but also to the same value coming from the Pareto front. Moreover, the *LSE* reduction is greater using the NiTiNOL than that obtained using the aluminum. The possibility of exploiting a large range of deformations allows us to achieve a meaningful improvement in the kinematic requirement, more than a conventional elastic material can provide. The third level of optimization can adapt a given topology to different materials.

The same refining process described here considering the NiTiNOL is repeated to adapt the same topology solution to different wing sections in the span direction.

5.4. Fourth Level

After collecting the optimal compliant structure solutions of different wing sections in the spanwise direction, the three-dimensional finite element model of the complete morphing leading edge device is generated. The model generation is based on Abaqus CAE coupled with the CST representation of the wing, via a Python interface. Abaqus is used to perform nonlinear stress analyses, verify the structural integrity of the final configuration under actuation and pressure loads, and finally evaluate the aeroelastic effects due to the wing-box interaction.

The complete model consists of a total of 20 compliant ribs connected to the stringers that are tied to the flexible skin. A full integration of stringers into the internal layers of the skin is assumed. This solution acts to minimize the local stiffness in the chord-direction introduced by the stringers, which provides a more localized actuation of the skin. It results in a more diffuse deformation and a reduction in the skin local waviness. The skin is divided into additional sections to avoid excessive discontinuities in the skin lamination. The smoother thickness distribution in the chordwise direction is also used to reduce the strain concentrations along the skin. Such regions are more representative of a technologically feasible solution, which can be developed when considering a smoother thickness variation due to a more progressive ply drop-off in the lamination of the skin. Constant layups are assumed in the span direction. The input actuation is introduced through a rotation of 80 deg of a shaft connected to all of the compliant ribs by a rigid kinematic chain. The aerodynamic loads are applied to the skin surface, while considering the pressure coefficient distributions of Figure 11. Pressures are applied once the final deflection has been achieved by a multi-step nonlinear analysis. The model consists of 73,822 elements: 67,600 linear 4-node shell (S4) elements for the skin modeling (46,306 for the external skin and 21,294 for the stringers) and 6222 linear 2-node beam (B31) elements for modeling the compliant ribs. As far as the skin is concerned, the element's typical size in the high curvature nose region is approximately 5 mm, whereas in the other regions, where the curvature variation is less significant, it is equal to 15 mm.

Three-dimensional stress analyses are based on the same solver used during the third level of optimization. The static implicit nonlinear multi-step analyses are performed by the Abaqus Standard-Implicit code. The stress field inside the compliant ribs is shown in Figure 19, and it is lower than the considered material strength, and, under the maximum actuation level, it perfectly matches the values computed during the third level of optimization.

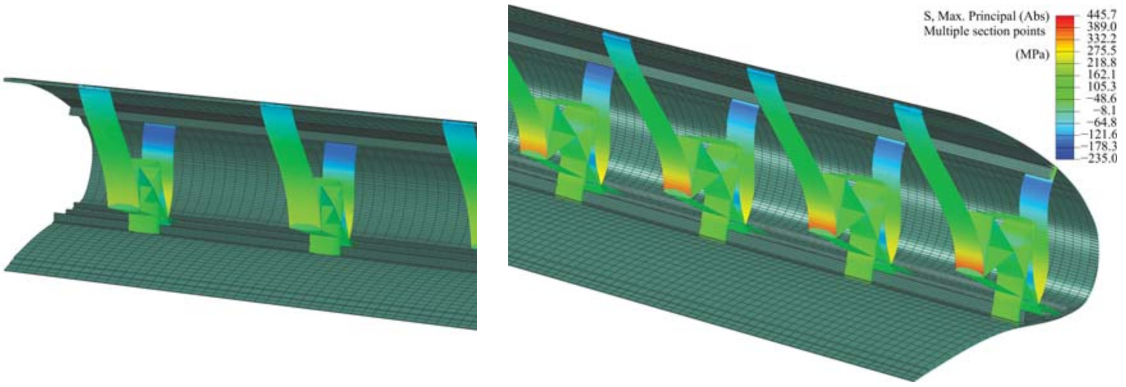

(**a**) (**b**)

Figure 19. Stress distribution inside the compliant ribs at the wing tip (**a**) and wing root (**b**).

The comparison between the target aerodynamic shape and the skin deformation is shown in Figure 20. The corresponding three-dimensional LSE value is equal to 5.32 mm. No anticlastic phenomena due to the actuation loads are observable, and the final solution shows a good shape quality that is not affected by any skin-waviness phenomena. Once the actuation shaft achieved the maximum droop nose configuration, the aerodynamic loads were not so important as to implicate a significant variation in the final shape. The highest deviations are detected in the nose regions where the skin is less supported and provides a lower relative bending stiffness.

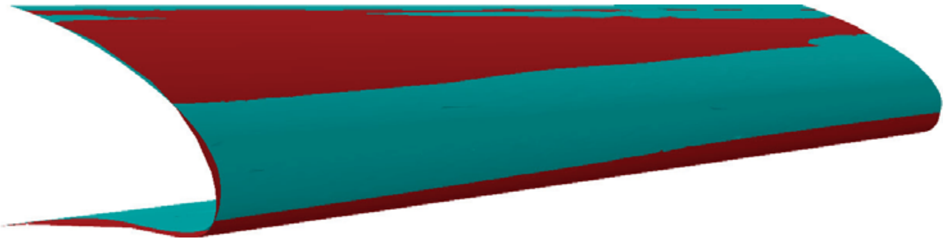

Figure 20. Comparison between deformation and the target shape.

The undeformed and maximum droop nose configuration are also given in Figure 21, which provides the strain distribution in the outermost layer of the skin. The strains show a very constant distribution in the spanwise direction, and the maximum strain value perfectly matches the skin structural constraints imposed in the first level of optimization. These results represent an important verification that confirms how the structural constraints used during the aerodynamic shape optimization allow us to simplify the design of the compliant structures without limiting their generality.

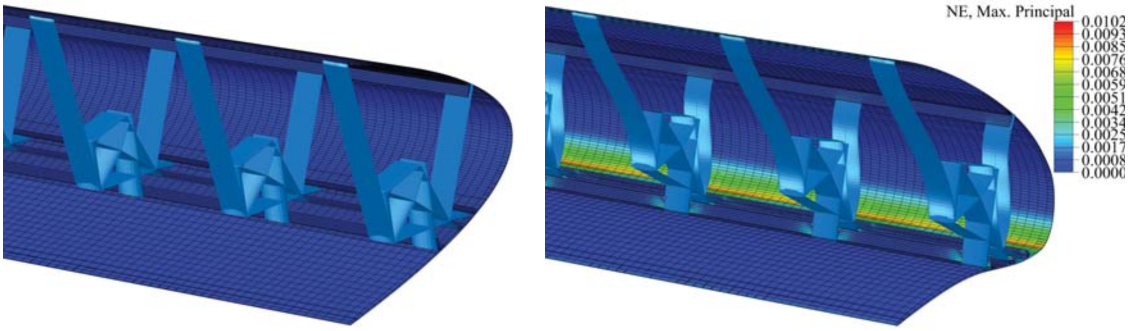

(**a**) (**b**)

Figure 21. Flexible skin deformation level along the undeformed (**a**) and the actuated (**b**) model.

Special attention must be focused on the impact of aeroelasticity on the correct functionality of the morphing leading edge device. Even the typical speeds related to these manoeuvres do not imply high aeroelastic deformation, and it is necessary to verify that the leading edge can maintain the requested deformed shape when the wing is aeroelastically deformed and that no skin buckling appears on the skin. To perform this evaluation, a simplified wing-box of the GRA has been modeled, which reproduces the same stiffness distribution as the real wing-box. According to the trim analysis results of the full aircraft, the same wing deformation in landing flight conditions is applied to the simplified wing-box, and then the morphing leading edge is actuated at the maximum requested for deployed configurations. As seen in Figure 22, the structural deformation does not impact on the maximum strain value computed on the skin. Moreover, Figures 23 and 24 show how the wing-box deformation does not affect the correct morphing leading edge deployment capability nor the accuracy of the deformed shape. It is possible to observe a small error in the upper skin area of the leading edge cross-sections placed from 60% to 100% of the span. In the other regions the two curves appear overlapped.

These simulations virtually assess that morphing devices realized with compliant structures are suitable to be coupled with wing-box structures. Unlike the rigid kinematics that represents hyperstatic structures, flexible systems introduce an additional degree of freedom into the structure, due to the flexibility, which can avoid further stress concentrations and avoid undesired coupling effects between the morphing device and the remainder of the structure.

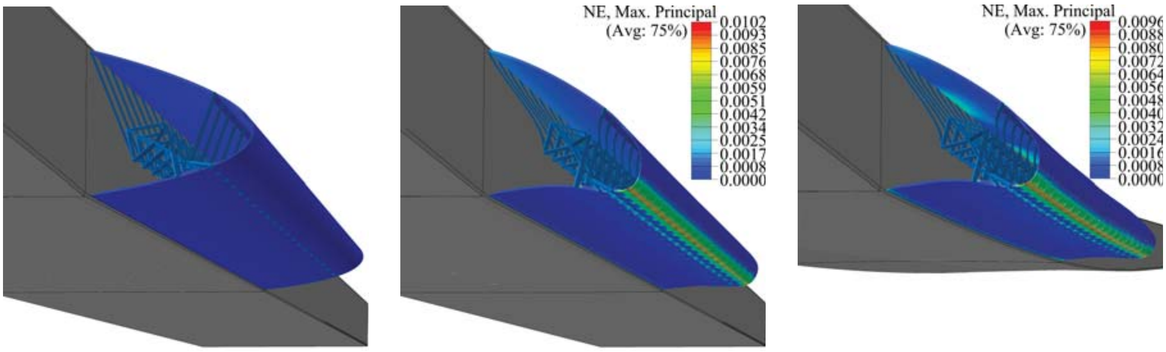

(**a**) (**b**) (**c**)

Figure 22. Virtual test: undeformed model (**a**); actuated leading edge model (**b**); deformed wing-box and actuated droop nose model (**c**).

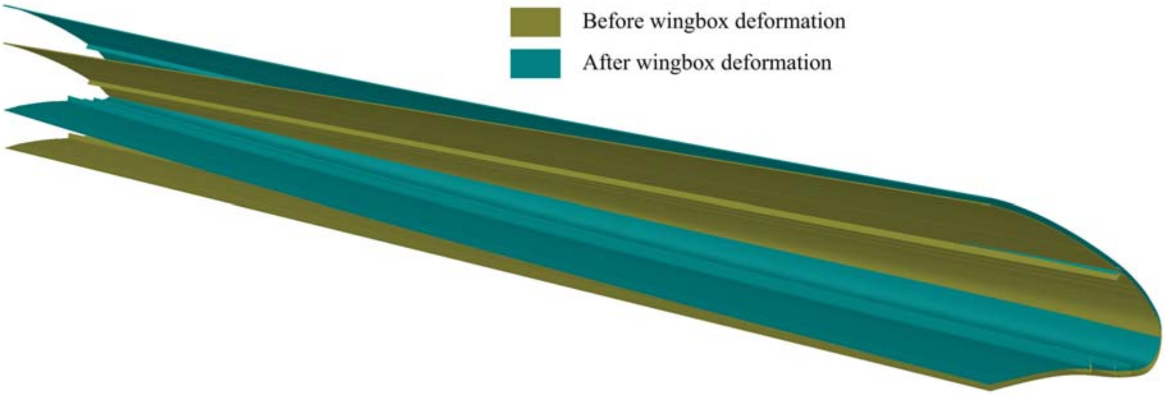

Figure 23. Leading edge deformation shape before and after the wing-box deformation.

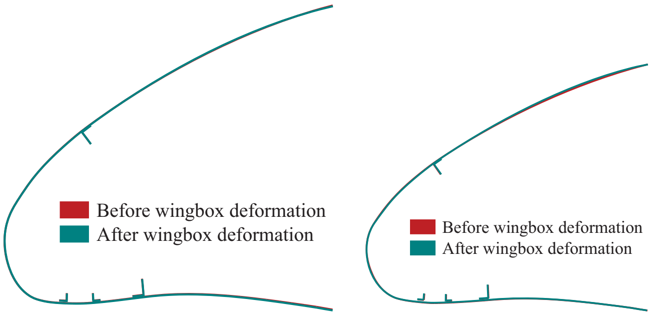

(**a**) (**b**)

Figure 24. Cross section deformation shape at 25% (**a**) and 75% (**b**) of the leading edge span.

6. Conclusions

This work proposed a multiobjective optimization problem for the design of morphing wing devices based on compliant structures. Due to the presence of conflicting requirements and multiple design load conditions, the final design point is found in the space of Pareto-optimal solutions. The design of compliant structures for aeronautical applications is based on a multilevel approach that enables us to solve multiobjective optimization problems in a rigorous way and a straightforward way. The entire design procedure has been applied to the design of a morphing leading edge device to be applied to an advanced regional aircraft. All of the results demonstrated the validity of the procedure according to its purposes of performance improvement, structural integrity, and versatility of applications. High-fidelity finite element analyses validate the whole procedure and confirmed the performances predicted during all of the design levels. Virtual tests show that the aeroelastic effects, also due to the wing-box deformation, do not compromise the correct functionality of the proposed morphing leading edge solution. Looking at the results, the LSEs values coming from the multilevel procedure are very small. However, the multilevel procedure is a sequential design approach that might lead to a compliant device which does not meet the set of target shapes. The designer can decide to perform additional aerodynamic computations to verify the final performances and to compare the aerodynamic results provided by the first level. When the performances are not acceptable, a different design point can be extracted from the Pareto-front and the third and fourth levels can be repeated.

The proposed optimization methodology is general and can be applied to the design of various active camber morphing wing devices that are based on compliant structures. Moreover, the design procedure can be applied to adapt an existing topology solution to the design of a scaled geometry, which can be used for experimental validations. The topology solution obtained in this work is currently used for the design of a smaller morphing leading edge to be installed on a 1:3 scale prototype of the GRA wing. Wind tunnel tests are planned in 2021 at Politecnico di Milano.

Finally, the acquisition of strong experience in the design of morphing devices by the proposed design procedure has proved to be fundamental to undertaking the difficult certification process of unconventional aircraft.

Supplementary Materials: The following are available online at http://www.mdpi.com/2076-3417/10/18/6380/s1, Figure S1: Upward deflection of an optimal compliant trailing edge solution; Figure S2: Downward deflection of an optimal compliant trailing edge solution; Figure S3: Twist deformation of the compliant trailing edge device.

Funding: The AirGreen2 Project has received funding from the Clean Sky 2 Joint Undertaking, under the European's Union Horizon 2020 research and innovation Programme, under grant agreement No. 807089.

Acknowledgments: Special thanks goes to Sergio Ricci who is a constant source of inspiration.

Conflicts of Interest: The author declares no conflict of interest.

References

1. Barbarino, S.; Bilgen, O.; Ajaj, R.M.; Friswell, M.I.; Inman, D.J. A Review of Morphing Aircraft. *J. Intell. Mater. Syst. Struct.* **2011**, *22*, 823–877. [CrossRef]
2. Barbarino, S.; Dettmer, W.G.; Friswell, M.I. Morphing trailing edges with shape memory alloy rods. In Proceedings of the 21st International Conference on Adaptive Structures and Technologies (ICAST), University Park, PA, USA, 4–6 October 2010.
3. Bowman, J.; Sanders, B.; Cannon, B.; Kudva, J.; Joshi, S.; Weisshaar, T. Development of next generation morphing aircraft structures. In Proceedings of the 48th AIAA/ASME/ASCE/AHS/ASC Structures, Structural Dynamics and Materials (SDM) Conference (AIAA 2007), Palm Springs, CA, USA, 4–7 May 2007.
4. McGowan, A.M.R.; Vicroy, D.D.; Busan, R.C.; Hahn, A.S. Perspectives on Highly Adaptive or Morphing Structures. In *Applied Vehicle Technology (AVT-168) Symposium on Morphing Vehicles*; NATO Research and Technology Organisation (RTO): Brussels, Belgium, 2009; pp. 1–14.
5. Weisshaar, T.A. Morphing Aircraft Technology–New Shapes for Aircraft Design. In *Multifunctional Structures/Integration of Sensors and Antennas Meeting (MP-AVT-141)*; NATO Research and Technology Organisation (RTO): Neuilly–sur–Seine, France, 2006; pp. 1–20.
6. Barbarino, S.; Pecora, R.; Lecce, L.; Concilio, A.; Ameduri, S.; De Rosa, L. Airfoil structural morphing based on SMA actuator series: Numerical and experimental studies. *J. Intell. Mater. Syst. Struct.* **2011**, *22*, 987–1004. [CrossRef]
7. Wright, J.R.; Cooper, J.E. *Introduction to Aircraft Aeroelasticity and Loads*; Wiley: Chichester, UK, 2007.
8. Lomax, T.L. *Structural Loads Analysis for Commercial Transport Aircraft*; AIAA, Inc.: Reston, VA, USA, 1996. [CrossRef]

9. Dharmasaroja, A.; Armstrong, C.G.; Murphy, A.; Robinson, T.T.; McGuinness, S.H.M.; Iorga, N.L.; Barron, J.R. Load Case Characterization for the Aircraft Structural Design Process. *AIAA J.* **2017**, *55*, 2783–2792. [CrossRef]
10. Krüger, W.; Klimmek, T. Definition of a Comprehensive Loads Process in the DLR Project iLOADS. In Proceedings of the Deutscher Luft- und Raumfahrtkongress 2016 (DLRK), Braunschweig, Germany, 13–15 September 2016.
11. Juretschke, I.R.; Blanco, M.C.; García, J.R.; Montes, J.H. Maneuver Loads Calculation via Optimization Techniques. In Proceedings of the 3rd CEAS Air & Space Conference and the 21st AIDAA Congress CEAS 2011: The International Conference of the European Aerospace Societies, Manchester, UK, 17–20 October 2011; pp. 1473–1482.
12. Román, J. A New Approach to the Aircraft Manoeuvre Loads Problem. In Proceedings of the CEAS 2009 European Air and Space Conference, Manchester, UK, 26–29 October 2009.
13. Beaverstock, C.S.; Woods, B.K.; Fincham, J.H.S.M.; Friswell, M.I. Performance Comparison between Optimised Camber and Span for a Morphing Wing. *Aerospace* **2015**, *2*, 524–554. [CrossRef]
14. Magrini, A.; Benini, E.; Ponza, R.; Wang, C.; Khodaparast, H.H.; Friswell, M.I.; Landersheim, V.; Laveuve, D.; Asins, C.C. Comparison of Constrained Parameterisation Strategies for Aerodynamic Optimisation of Morphing Leading Edge Airfoil. *Aerospace* **2019**, *6*, 31. [CrossRef]
15. Li, D.; Zhao, S.; Da Ronch, A.; Xiang, J.; Drofelnik, J.; Li, Y.; Zhang, L.; Wu, Y.; Kintscher, M.; Monner, H.P.; et al. A review of modelling and analysis of morphing wings. *Prog. Aerosp. Sci.* **2018**, *100*, 46–62. [CrossRef]
16. Sodja, J.; Martinez, M.J.; Simpson, J.C.; De Breuker, R. Experimental evaluation of a morphing leading edge concept. *J. Intell. Mater. Syst. Struct.* **2019**, *30*, 2953–2969. [CrossRef]
17. Rivero, A.E.; Weaver, P.M.; Woods, B.K. Structural Modelling of Compliance-Based Morphing Structures under Transverse Shear Loading. In Proceedings of the AIAA Scitech 2019 Forum, San Diego, CA, USA, 7–11 January 2019.
18. Rudenko, A.; Hannig, A.; Monner, H.P.; Horst, P. Extremely deformable morphing leading edge: Optimization, design and structural testing. *J. Intell. Mater. Syst. Struct.* **2018**, *29*, 764–773. [CrossRef]
19. Kota, S.; Flick, P.; Collier, F.S. Flight Testing of FlexFloil$^{\mathrm{TM}}$ Adaptive Compliant Trailing Edge. In Proceedings of the 54th AIAA Aerospace Sciences Meeting, AIAA Scitech Forum 2016, San Diego, CA, USA, 4–8 January 2016. [CrossRef]
20. De Gaspari, A.; Ricci, S.; Antunes, A.; Odaguil, F.; Lima, G. Chapter 6: Expected Performances. In *Morphing Wing Technologies–Large Commercial Aircraft and Civil Helicopters*; Butterworth–Heinemann: Oxford, UK, 2018; pp. 175–203. [CrossRef]
21. De Gaspari, A.; Riccobene, L.; Ricci, S. Design, Manufacturing and Wind Tunnel Validation of a Morphing Compliant Wing. *J. Aircr.* **2018**, *55*, 2313–2326. [CrossRef]
22. Santer, M.; Pellegrino, S. Topological Optimization of Compliant Adaptive Wing Structure. *AIAA J.* **2009**, *47*, 1080–1091. [CrossRef]
23. De Gaspari, A.; Ricci, S. A Two–Level Approach for the Optimal Design of Morphing Wings Based On Compliant Structures. *J. Intell. Mater. Syst. Struct.* **2011**, 22, 1091–1111. [CrossRef]
24. Deb, K. *Multi–Objective Optimization Using Evolutionary Algorithms*; John Wiley & Sons, Inc.: New York, NY, USA, 2009.
25. Kirn, J.; Storm, S. Kinematic solution for a highly adaptive droop nose In Proceedings of the 25th International Conference on Adaptive Structures and Technologies (ICAST), The Hague, The Netherlands, 6–8 October 2014.
26. Kintscher, M.; Monner, H.P.; Heintze, O. Experimental testing of a smart leading edge high lift device for commercial transportation aircrafts. In Proceedings of the 27th International Congress of the Aeronautical Sciences (ICAS), Nice, France, 19–24 September 2010.
27. Miettinen, K. *Nonlinear Multiobjective Optimization*; Kluwer Academic: Norwell, MA, USA, 1999.
28. Lu, K.J.; Kota, S. Topology and Dimensional Synthesis of Compliant Mechanisms Using Discrete Optimization. *J. Mech. Des.* **2006**, *128*, 1080–1091. [CrossRef]
29. Shield, R.T.; Prager, W. Optimal Structural Design for Given Deflection. *J. Appl. Math. Phys. ZAMP* **1970**, *21*, 513–523. [CrossRef]
30. Sigmund, O.; Bendsøe, M.P. *Topology Optimization: Theory, Methods and Applications*; Springer: Berlin/Heidelberg, Germany, 2003.

31. Frecker, M.; Kikuchi, N.; Kota, S. Topology optimization of compliant mechanisms with multiple outputs. *Struct. Optim.* **1999**, *17*, 269–278. [CrossRef]
32. Pedersen, C.B.W.; Buhl, T.; Sigmund, O. Topology Synthesis of Large–displacement Compliant Mechanisms. *Int. J. Numer. Methods Eng.* **2001**, *50*, 2683–2705. [CrossRef]
33. Kulfan, B.M. Universal Parametric Geometry Representation Method. *J. Aircr.* **2008**, *45*, 142–158. [CrossRef]
34. De Gaspari, A.; Ricci, S. Knowledge–Based Shape Optimization of Morphing Wing for More Efficient Aircraft. *Int. J. Aerosp. Eng.* **2015**, *2015*, 325724. [CrossRef]
35. Sigmund, O. On the design of compliant mechanisms using topology optimization. *Mech. Struct. Mach.* **1997**, *25*, 493–524. [CrossRef]
36. Ghiringhelli, G.L.; Masarati, P.; Mantegazza, P. Multibody Implementation of Finite Volume C^0 Beams. *AIAA J.* **2000**, *38*, 131–138. [CrossRef]
37. Cavalieri, V.; De Gaspari, A.; Ricci, S. Optimization of compliant adaptive structures in the design of a morphing droop nose. *Smart Mater. Struct.* **2020**, *29*, 22. [CrossRef]
38. Corporation, D. *Abaqus Scripting User's Guide*; Dassault Systemes Simulia Corporation: Velizy Villacoublay, France, 2016.
39. De Gaspari, A.; Moens, F. Aerodynamic Shape Design and Validation of an Advanced High-Lift Device for a Regional Aircraft with Morphing Droop Nose. *Int. J. Aerosp. Eng.* **2019**, *2019*, 7982168. [CrossRef]
40. Qidwai, M.; Lagoudas, D. On thermomechanics and transformation surfaces of polycrystalline NiTi shape memory alloy material. *Int. J. Plast.* **2000**, *16*, 1309–1343. [CrossRef]